Silicon nitride as anode material for Li-ion batteries: Understanding the SiN$_x$ conversion reaction

Asbjørn Ulvestad[a,b,*], Jan Petter Mæhlen[a], Martin Kirkengen[a,c]

[a] *Department of Battery Technology, Institute for Energy Technology, P.O. Box 40, NO-2027, Kjeller, Norway*
[b] *Department of Physics, Centre for Materials Science and Nanotechnology, University of Oslo, P.O. Box 1048 Blindern, NO-0316, Oslo, Norway*
[c] *Department of Technology Systems, University of Oslo, P.O. Box 70, NO-2027, Kjeller, Norway*

HIGHLIGHTS

- A model reaction is developed to describe the SiN$_x$ conversion reaction.
- This model is fitted to cycling data from amorphous SiN$_x$ thin film electrodes.
- The conversion is determined to result in cyclable silicon in a Li$_2$SiN$_2$ matrix.
- The bulk capacity and reversibility of SiN$_x$ of any given composition is predicted.
- The matrix is found to slowly delithiate at potentials exceeding ~0.5 V vs. Li$^+$/Li.

GRAPHICAL ABSTRACT
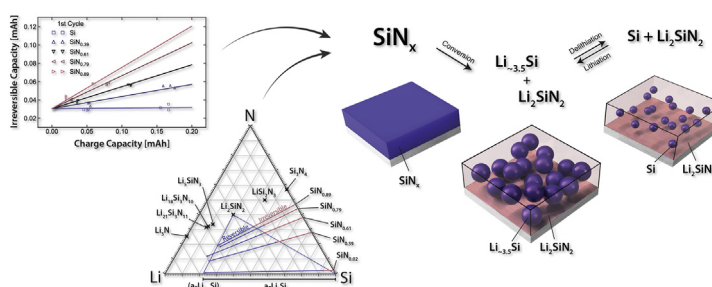
ARTICLE INFO

ABSTRACT

An extensive research effort is being made to develop the next generation of anode materials for lithium ion batteries. A large part of this effort has been related to silicon, primarily due to its considerable theoretical capacity; however, very limited cycling stability has prevented widespread commercial adoption. A potential solution for this is to use convertible sub-stoichiometric silicon nitride (a-SiN$_x$), which goes through an irreversible conversion reaction during the initial lithiation cycle, producing active silicon domains in an inactive, lithium conducting matrix. Relative to pure silicon, the resulting composite material has gained cycle life at the cost of reduced specific capacity. The specifics of the conversion reaction, however, have not yet been determined; hence, the impact of varying nitrogen content remains uncertain. In this work we develop a model reaction which relates the reversible and irreversible capacities of an electrode to the composition of the conversion products. By fitting this model to experimental data from a large number of a-SiN$_x$ thin film electrodes with different thickness and composition, we determine with a high probability that the matrix composition is Li$_2$SiN$_2$. From this, the reversible and irreversible capacities of the material can be predicted for a nitride of a given composition.

1. Introduction

The invention of the lithium ion battery has been one of the key factors in enabling the revolution of portable electronic devices seen over the last decades. Increasing power-demands of these devices, as well as the incorporation of Li-ion batteries in electric vehicles place ever higher demands on the batteries. This has led to a significant research effort into the development of new electrode materials with

---

improved volumetric and specific capacity, cycle life and rate capability, which do not compromise on safety. For Li-ion batteries, silicon has attracted a lot of attention as anode material due to its very high specific capacity (3579 mAh/g) compared to that of the commonly used carbonaceous anodes (372 mAh/g) [1]. Silicon does, however, have several issues related to the large volume change the material undergoes during cycling. Attempts to resolve these issues are generally based on what is termed dimensional stabilization – using nanostructured materials to reduce internal stress formation [2–17]. The very large specific surface areas of these nanostructures present a number of new problems, which have called for further research on surface modification and coatings [12,18–24].

A class of materials which are not necessarily nanostructured but inherently utilize dimensional stabilization is commonly known as in-situ convertible oxides [25–27]. These materials rely on an irreversible conversion reaction during the first lithiation cycle which causes a phase separation of a finely dispersed active alloy component and an inactive matrix component [28]. This reaction was first described for the tin based composite oxide electrode in a report by Fuji Photo Film Co. in 1997 [26], and have later been extended to silicon sub-oxides (SiO_x) [29–31]. There have also been reports on different nitrides undergoing reversible electrochemical reactions with lithium, with a wide variety of different reaction mechanisms. Several ternary nitrides, e.g. Li_3FeN_2 [32] and Li_7MnN_4 [33], are assumed to function by reversible reconstitution reactions. Some binary nitrides M_3N (M = Co, Fe, Ni) have been shown to function by partially reversible displacement reactions on the form $M_3N + Li = M + Li_3N$ [34,35]. Others again, like Sn_3N_4 [36] and Ge_3N_4 [37], function along the same lines as the convertible oxides, with the reversible capacity stemming from the lithiation and delithiation of the metal formed during conversion. Titanium nitride (TiN), on the other hand, is regarded as inactive, and has instead been used as a structural stabilizer and conductive component [38,39].

Silicon nitride was initially regarded as an inactive material in the context of lithium ion batteries, and has been used as an inactive scaffolding material for silicon based anodes [40]. However, in the last decade, several groups have reported reversible charge-discharge behavior of silicon nitrides of different compositions and crystallinity [23,41–46], albeit with varying performance. As the properties of the silicon nitride in these works differ in many aspects, a direct comparison of the reported results can hardly be made. While most are of the opinion that a conversion type reaction is taking place, there is disagreement as to what the products of said reaction are; whether it is lithiated silicon and lithium nitride (Li_3N) [42,46], lithiated silicon, silicon nitride (Si_3N_4) and Li_3N [41], or lithiated silicon and a ternary lithium silicon nitride (Li_2SiN_2) [44].

Understanding the conversion reaction allows targeted tailoring of the material properties, and is crucial for the continued development of this electrode system. The purpose of this work has therefore been to investigate the first cycle conversion reaction by comparing the performance of different substoichiometric amorphous nitrides (a-SiN_x) cycled under comparable conditions. Here we introduce a model which, when fit to experimental results, allows the separation of surface and bulk losses; and moreover, an estimation of the matrix phase composition. Using this model in conjunction with experimental measurements from a large number of different SiN_x thin film electrodes of varying composition and thickness, the composition of the matrix has been estimated to be approximately Li:Si:N 2:1:2. Furthermore, by analysis of the matrix delithiation at higher voltages, we have shown that the matrix in all probability consists of a single phase, Li_2SiN_2, rather than a combination of Li_3N and Si_3N_4. This information enables us to predict the reversible and irreversible capacities of an amorphous silicon nitride of any given composition.

2. Materials and methods

The model derived in this work is fitted to experimental data

obtained from a number of amorphous silicon nitride thin film electrodes. The long term cycling performance and degradation mechanisms of these films have been the subject of previous publications [47,48], in which a thorough characterization of the films can be found; hence this paper will only contain a brief summary of the characterization results, necessary for a proper evaluation of the model. The thin film electrodes were prepared by plasma enhanced chemical vapor deposition (PECVD, Oxford Instruments Plasmalab System133), with silane (SiH_4) and ammonia (NH_3) as precursors. The films were deposited on rolled copper substrates, and different compositions were obtained by varying the flow rate of the precursor gasses in the plasma. The silane flow rate was held at 25 sccm, while the ammonia flow rate was varied from 0 to 40 sccm in 10 sccm intervals, resulting in films of five different compositions. Different thicknesses were made by depositing for different durations. Of the most nitrogen rich composition five different thicknesses were made, nominally 40 nm, 80 nm, 120 nm, 160 nm, and 200 nm, while the other four compositions were made in two thicknesses, nominally 40 nm and 120 nm.

The surface morphology and coverage of the pristine films were characterized using optical microscopy and scanning electron microscopy (SEM, Hitachi TM3000 & JEOL JIB-4500). The thicknesses of the films were measured using spectroscopic ellipsometry (V-VASE® J.A. Woollam Co.), which was conducted on films simultaneously deposited on polished silicon wafers, as it requires a smooth surface. Selected films were also characterized using transmission electron microscopy (TEM) using a monochromated and probe corrected FEI Titan G2 60–300 operated at 300 kV in both projection and scanning TEM mode (STEM). For this analysis cross section TEM samples were prepared from the films using a Jeol JIB-4500 focused ion beam (FIB) system. The compositions of the films were determined using X-ray photoelectron spectroscopy (XPS) analysis, which was conducted on a Kratos Axis Ultra DLD spectroscope using monochromated Al Kα X-rays (1486.6 eV). Any surface contamination was removed by argon sputtering at 2 kV and 100 μA for 2 min before characterization. The densities of the films were estimated using the characteristic bulk plasmon energy as measured in the TEM using electron energy loss spectroscopy (EELS). Detailed descriptions of these analyses can be found in Ulvestad et al. [47] and Ulvestad et al. [48].

Electrochemical testing was performed using Ø15 mm electrodes mounted in 2032 coin cells against a lithium metal counter electrode, separated by a Celgard 3401 separator. The electrolyte used consisted of 1 M $LiPF_6$ in ethylene carbonate (EC)/propylene carbonate (PC)/dimethyl carbonate (DMC) (1:1:3 by mass), with 1 wt.% vinylene carbonate (VC) and 5 wt.% fluoroethylene carbonate (FEC) additives. The cells were assembled in an argon filled glove box with $O_2 < 0.1$ ppm and $H_2O < 0.1$ ppm, and cycled using an Arbin BT-2000 galvanostat/potentiostat at ambient temperature. Cycling was conducted galvanostatically between 0.05 V vs. Li^+/Li and 1 V vs. Li^+/Li unless otherwise indicated.

3. Results and discussion

3.1. Characterization of the pristine SiN_x films

Table 1 gives an overview of the measured thicknesses, compositions and densities of the different thin films. Films deposited using the same process parameters are assumed to have the same composition and density. Compositions were determined using XPS to range from pure a-Si to a-$SiN_{0.89}$. This analysis was conducted on the 40 nm and 120 nm films, and the average value was used for each composition. Density determination from TEM-EELS measurements were conducted on the 120 nm films of each composition. As a confirmation of this method's applicability, the same measurements and analysis were conducted on samples of pure crystalline silicon and stoichiometric c-Si_3N_4 (Sigma Aldrich). The densities of these samples were determined to be 2.38 g/cm³ and 3.24 g/cm³, respectively, which, compared to the

Table 1
Film parameters determined by ellipsometry, TEM and XPS, summarized from Ulvestad et al. [47] and Ulvestad et al. [48].

Composition	Thickness [nm]			Refractive index	Composition, x = [N]/[Si]		Density, [g/cm³]
	Target	Measured, ellipsometry	Measured, TEM	Ellipsometry n (630 nm)	XPS	XPS, avg.	ρ_p [a]
A	40	42.3 ± 0.8		4.28	0.02	0.02	2.17
A	120	124.1 ± 0.9		4.33	0.02		
B	40	55.9 ± 0.1		3.31	0.38	0.39	2.15
B	120	176.6 ± 0.5	180	3.24	0.40		
C	40	46.5 ± 0.1		2.78	0.59	0.61	2.25
C	120	127.5 ± 0.3	130	2.82	0.63		
D	40	40.0 ± 0.1		2.47	0.79	0.79	2.31
D	120	133.6 ± 1.1	135	2.45	0.78		
E	40	40.9 ± 0.4		2.24	0.91	0.89	2.44
E	80	79.5 ± 0.1		2.35			
E	120	114.2 ± 0.1	116	2.37	0.87		
E	160	155.2 ± 0.3		2.38			
E	200	190.2 ± 0.7		2.27			

[a] Calculated using the bulk plasmon energy measured using STEM-EELS, as described in Ulvestad et al. [47].

tabulated values of 2.33 g/cm³ and 3.19 g/cm³, are within the expected margin of error for such experiments. The densities were found to be similar for all the films, as seen in Table 1, showing a slight increase with increasing nitrogen content, as expected.

The film thicknesses were determined by ellipsometry to be generally close to the nominal values, with the exception of the a-SiN$_{0.39}$ films, which were somewhat thicker. While this is expected to impact their long term cycling stability, it should not impact their applicability for the model. Using STEM imaging, it was confirmed that the thickness determination by ellipsometry conducted on the films deposited on silicon wafers can be extended to the films simultaneously deposited on the copper substrates. A comparison of measurements from ellipsometry and STEM for selected films can also be seen in Table 1.

Visual inspection, optical microscopy, SEM and TEM were used in conjunction to examine the film on the macro, micro and nano scales. The optical and SEM micrographs in Fig. 1, while dominated by the structure of the underlying copper substrates, show that the film coverage was even, with no sign of island formation. Due to interference effects, the color of the film is sensitive to the film thickness, hence visual inspection and optical microscopy was able to determine that the thickness of the film was uniform over several centimeters down to the micron scale. On the micron to nano scale, STEM imaging confirmed that the films were dense and had even thickness, despite the relative roughness of the substrates.

Peak fitting of the XPS Si 2p peak by a method described by Ingo et al. [49] allows determination of the distribution of silicon atoms in different coordination states/tetrahedra: Si-Si$_4$, Si-Si$_3$N, Si-Si$_2$N$_2$, Si-SiN$_3$ and Si-N$_4$. As previously shown for the films used in this work [47,48], this analysis revealed that the fraction of silicon atoms in a Si-Si$_4$ coordination was significantly larger than what is expected if the atoms are randomly distributed, indicating that there is some phase segregation of pure silicon. This was confirmed using STEM imaging, as

seen in Fig. 1, which revealed the formation of clusters with sizes up to approximately 10 nm. Formation of silicon clusters in silicon rich a-SiN$_x$ have previously been reported by Volodin et al. [50], Park, et al. [51], and Gritsenko et al. [52]. Since a redistribution of nitrogen is expected to occur during the initial conversion reaction of this material in any case, this is not expected to have a noteworthy effect on the final state of the electrodes and thus the applicability of the model. It may, however, affect the rate at which this state is approached, thus underlining the importance of using a low current rate.

3.2. Analysis of the conversion reaction

While there is a general agreement that one of the products of the conversion reaction of silicon nitride is lithiated silicon, the composition of the remaining material has not been conclusively determined in earlier reports. Yamane et al. [53] reported on the thermal formation of different ternary lithium silicon nitrides from Si$_3$N$_4$ and Li$_3$N, giving reason to believe that the formation of a ternary phase is energetically favorable. Based on this premise, we propose that a chemical equation of the following form best describes the initial reduction reaction:

$$n\,SiN_x + y\,Li^+ + ye^- \rightarrow na\,Li_{3.5}Si + n\,Li_bSi_{1-a}N_x + cA\,Li^{SEI} \qquad (1)$$
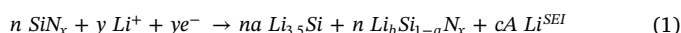
We have constructed this reaction for a thin film system, hence the surface area of the electrodes is assumed to remain constant, regardless of the film thickness. The final term, related to lithium lost in the formation of the solid electrolyte interphase (SEI), is thus independent of the thickness of the film (expressed here as moles of SiN$_x$, n, related to the film thickness, t, by $n = At/V_m$, where V_m is the molar volume and A is the electrode area). Note that Li$_{3.5}$Si is used as the composition of the fully lithiated silicon, rather than the conventionally used Li$_{3.75}$Si. This value is chosen because the cells are lithiated with a cut-off at 0.05 V vs. Li$^+$/Li, which, as shown by Ogata et al. [54], largely avoids the formation of c-Li$_{3.75}$Si.
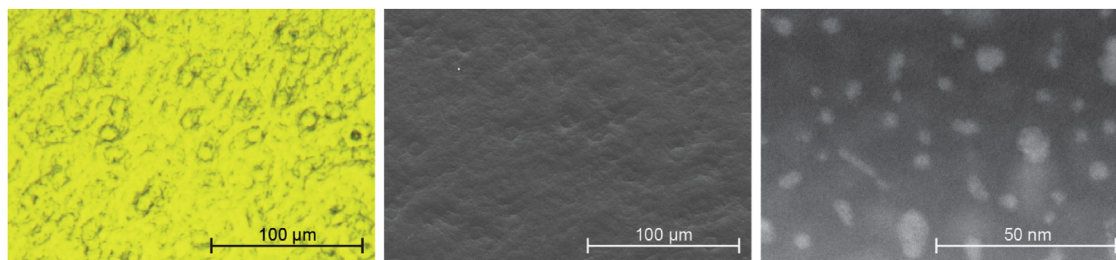

Fig. 1. Plane view optical (left) and SEM (middle) micrographs of the 156 nm SiN$_{0.89}$ film. The structure of the surface is related to the structure of the rolled copper substrate. The uniform color in the optical micrograph indicates a uniform film thickness. STEM image of the 176 nm SiN$_{0.39}$ film (right), showing the segregation of nano-scale inhomogeneities. (For interpretation of the references to color in this figure legend, the reader is referred to the Web version of this article.)

We assume that the lithium silicide phase ($Li_{3.5}Si$) provides all the reversible capacity, while the formation of the ternary compound and the SEI is irreversible. Given that the conversion happens to completion during the initial lithiation of the electrode, the first cycle discharge/lithiation capacity (Q_{DC}), charge/delithiation capacity (Q_C) and irreversible capacity (Q_I) can be expressed by

$$Q_{DC} = 3.5naF + nbF + cAF = \left[\frac{(3.5a + b)F}{M_{Si} + xM_N}\right]m + cAF \tag{2}$$

$$Q_C = 3.5naF = \left[\frac{3.5aF}{M_{Si} + xM_N}\right]m \tag{3}$$

$$Q_I = nbF + cAF = \left[\frac{bF}{M_{Si} + xM_N}\right]m + cAF \tag{4}$$

Here $m = n(M_{Si} + x*M_N)$, where m is electrode mass, M_{Si} and M_N are the molar masses of silicon and nitrogen, respectively, and F is Faradays constant. Equations (2)–(4) are all linearly dependent on mass, and the proportionality constants (brackets) thus represent the bulk material contributions to the discharge, charge and irreversible capacities, respectively. The value of these terms can then be determined by comparing electrodes of the same composition but with different thickness/mass.

Similarly, the Coulombic efficiency (η_C) can be expressed by:

$$\eta_C = \frac{Q_C}{Q_{DC}} = \frac{3.5naF}{3.5naF + nbF + cAF} = \frac{3.5a}{3.5a + b} * \frac{n}{n + \frac{cA}{3.5a + b}} \tag{5}$$

The first factor of the final equation describes the ratio between the amounts of reversibly stored lithium and total lithium in the two bulk phases, while the second factor describes the relation between the lithium lost during SEI formation and the lithium stored in the bulk. From equation (5) it is evident that as the thickness, and thus n, increases, the second factor approaches unity and surface effects become negligible. The first factor then describes the theoretical maximum first cycle Coulombic efficiency of the bulk material.

Fig. 2a shows the first cycle discharge capacity, charge capacity and irreversible capacity as functions of electrode mass for a-$SiN_{0.89}$ electrodes with five different thicknesses (41 nm, 80 nm, 114 nm, 156 nm, and 190 nm), the long term cycling performance of which can be found elsewhere [47]. Least squares fittings of equations (2)–(4) to these data yield a bulk specific discharge capacity of 1796 mAh/g, a reversible capacity of 1230 mAh/g and an irreversible capacity of 566 mAh/g for of $SiN_{0.89}$, respectively. This analysis also determined the surface loss to be 0.0362 mAh, or 20.5 μA h/cm². From Fig. 2a it is evident that these linear functions are well suited to express the different capacities for different thicknesses, and thus corroborate the assumption that the surface area is constant. In terms of the parameters a and b introduced in equation (1), the values obtained in this fitting correspond to $a = 0.535$ and $b = 0.860$, which for [N]/[Si] = 0.89 results in a matrix phase composition of $Li_{0.96}Si_{0.52}N$. This composition is close to Li_2SiN_2, one of the known stable compounds in the ternary lithium-silicon-nitride system, and is in agreement with the findings of Suzuki et al. [44]. It has also been reported that Li_2SiN_2 is the only phase which forms from Si_3N_4 in liquid lithium at 600 °C [55], indicating that it is indeed one of the more readily formed phases of the Li-Si-N ternary system. Relative to this phase, the matrix is slightly lithium deficient and with a silicon abundance. The corresponding fitting of equation (5) to the experimentally measured 1st cycle Coulombic efficiencies is displayed in Fig. 2b. The best fit parameters result in a theoretical maximum Coulombic efficiency of $SiN_{0.89}$ of 69.5%.

The accuracy of fitting equations (2)–(5) to experimental data is necessarily dependent on the correct determination of the electrode mass. Since accurately determining the density of thin films can be challenging, it would be beneficial to eliminate the mass from these equations. This can be accomplished by combining equations (3) and
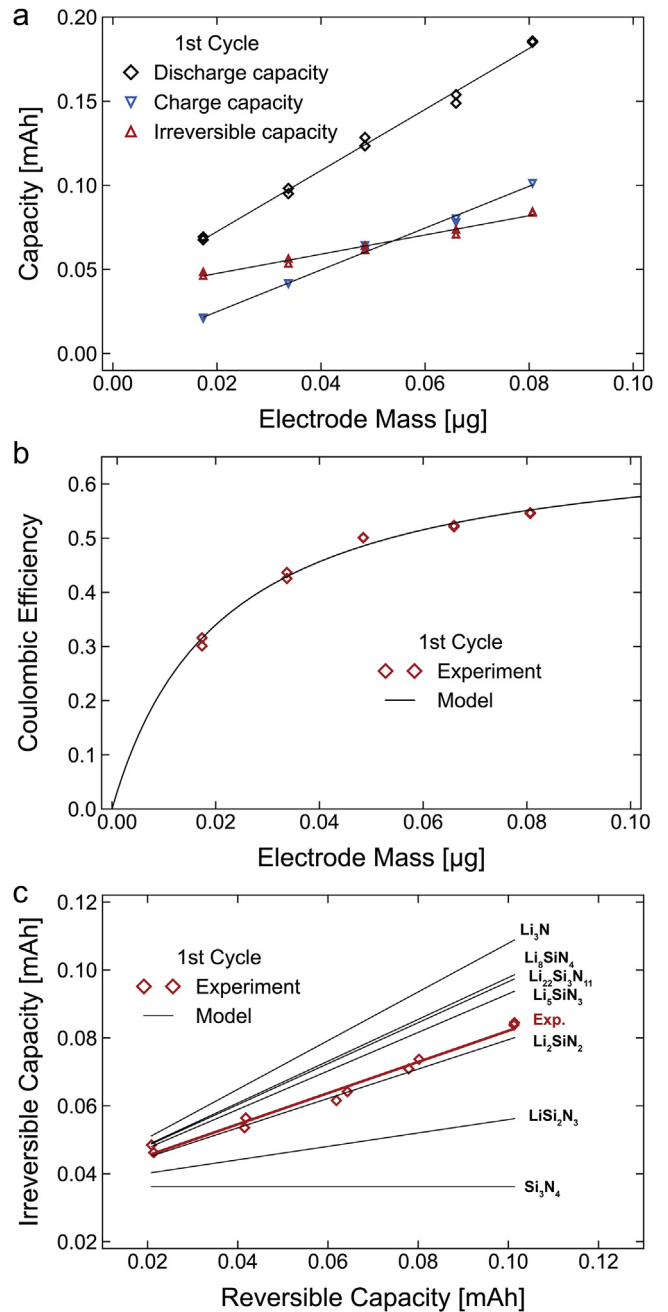
Fig. 2. a) Measured 1st cycle discharge, charge and irreversible capacities as functions of mass for the different $SiN_{0.89}$ electrodes (markers), and linear trends (lines). b) Coulombic efficiency as function of mass for the different $SiN_{0.89}$ electrodes (markers) and the corresponding least squares fit of Eq. (5) (line). c) The expected 1st cycle irreversible capacity of $SiN_{0.89}$ for different matrix phase compositions as functions of reversible capacity (black lines), together with the experimental data (red markers) and linear trend (red line). (For interpretation of the references to color in this figure legend, the reader is referred to the Web version of this article.)

(4), resulting in an expression for the irreversible capacity as a function of the charge capacity:

$$Cap_{irrev} = \left[\frac{b}{3.5a}\right]Cap_{rev} + cAF \tag{6}$$

This expression results in a system where a and b cannot be determined directly from experimental data from cells with the same composition. It can, however, be used to compare experimental data with reactions in which the matrix composition is one of the known ternary lithium

silicon nitrides phases, for which a and b are known. As can be seen in Fig. 2c, this comparison for the $SiN_{0.89}$ electrodes support the previous result that the matrix composition is close to Li_2SiN_2.

If, however, we compare electrodes with both different thickness *and* composition, we can expand Eq. (6) by defining two values k_1 and k_2 as the molar ratios of silicon to nitrogen and lithium to nitrogen in the matrix phase, respectively, so that

$$k_1 = \frac{1-a}{x} \quad \rightarrow \quad a = 1 - k_1 x \tag{7}$$

and

$$k_2 = \frac{b}{x} \quad \rightarrow \quad b = k_2 x \tag{8}$$

By substituting these expressions for a and b in Eq. (6), we obtain

$$Cap_I = \frac{k_2 x}{(1 - k_1 x) \, 3.5} \, Cap_C + cAF \tag{9}$$

In a multi-phase system close to equilibrium, lithiation to a given electrochemical potential is expected to result in a certain combination of phases, with the nitrogen content of the initial nitride determining the relative amount of the phases. The factors k_1 and k_2 are then expected to be common for nitrides of varying composition, and can therefore be determined, together with c, by fitting equation (9) to experimental data for nitrides with a range of compositions *and* thicknesses. This holds as long as diffusion limitations and Ohmic voltage drop are negligible, hence a low current rate should be used during this cycle. Fig. 3 shows the least squares fitting of equation 13 to the experimentally measured first cycle charge capacity and irreversible capacity acquired from 28 cells of five different compositions (a-$SiN_{0.89}$, a-$SiN_{0.79}$, a-$SiN_{0.61}$, a-$SiN_{0.39}$ and pure a-Si), each of two different thicknesses, cycled at a current rate of C/20 (the long term cycling performance of these cells are published in Ref. [48]). This analysis resulted in the best fit parameters $k_1 = 0.52$ and $k_2 = 0.94$, corresponding to a matrix composition of $Li_{0.94}Si_{0.52}N$. This analysis shows the same slight silicon abundance as was determined from the mass dependent analysis performed for a-$SiN_{0.89}$ electrodes of different thickness, but with a somewhat more pronounced lithium deficiency.

The differential capacity analysis of the 100th cycle for a number of SiN_x electrodes can be seen in Fig. 4. The primary silicon lithiation peaks, Si#d1 and Si#d2, are tagged in the figure. As determined by Key et al. [56], Si#d1 is related to the lithiation of the a-Si matrix to a composition of approximately a-$Li_{2.0}Si$, retaining some silicon-silicon interaction. Si#d2 is related to the formation of a-$Li_{3.5}Si$ from a-$Li_{2.0}Si$, largely isolating the silicon atoms [54,56,57]. In addition to these, another lithiation peak, M#d1, which does not occur in silicon thin films, appear gradually as the nitrogen content is increased, and is therefore attributed to a lithiation of the matrix. It does account for only a small fraction of the total capacity, even for the most nitrogen rich films; nonetheless, considering that in the development of the model it was assumed that the lithium silicide was the only active phase, it is obvious that the activity of the matrix, albeit limited, will have implications for the result. A partial matrix delithiation would result in a

higher-than-expected measured reversible capacity, and therefore also a decreased calculated irreversible capacity, resulting in an underestimation of both the lithium and silicon content of the matrix phase. On one hand, this would account for the previously estimated lithium deficiency relative to Li_2SiN_2. On the other hand, it also means that the silicon abundance is likely to be somewhat larger than estimated; however, the reversible capacity did increase slightly in the cycles following the conversion, which would, at least partially, counterbalance this. It should also be noted that the solid state conversion is expected to produce a very finely dispersed phase distribution with a considerable interface area, the effects of which are difficult to predict.

From these analyses it has been shown that the matrix composition is close to Li_2SiN_2; however, this does not inherently exclude the possibility that the matrix is a mixture of Li_3N and Si_3N_4, as was proposed by Ahn et al. [41]. If we, for the sake of argument, assume that the current rate is low enough for the lithiation and delithiation to be regarded as quasi-static, the phase distribution of the electrode can be displayed in a phase diagram. Fig. 5 shows a constructed quasi-equilibrium Li-Si-N ternary phase diagram, which includes a-Li_xSi, Si_3N_4 and Li_3N, in addition to the known stable ternary phases. The expected lithiation pathways of the different a-SiN_x compositions can also be seen in this figure. The blue and red parts of the lithiation paths correspond to the reversible and irreversible bulk capacity contributions, respectively, as found by fitting equations (3) and (4) to the cells of each composition. The endpoints of the reversible lithiation and delithiation shows that cycling between 0.05 V and 1 V vs. Li^+/Li most likely happens in the two-phase area $Li_2SiN_2 + Li_xSi$, by lithiation and delithiation of the a-Li_xSi. This process is then limited by the tie lines between $Li_2SiN_2 + Si$ and $Li_2SiN_2 + $ a-$Li_{3.5}Si$ (blue lines in Fig. 5), as hypothesized. From a thermodynamic point of view, these limits would not exist if the matrix consisted of both Li_3N and Si_3N_4, in which case further lithiation would then necessarily lead to the continued formation of Li_3N and $Li_{3.5}Si$ at the cost of Si_3N_4. Since this entails no change in the composition of the phases, but rather their relative fractions, there is no change in potential; hence this reaction would continue until the electrode consisted only of Li_3N and $Li_{3.5}Si$. Even though this rationale disregards kinetic limitations, given the low current rate and small film thickness used in the experiments, it is a strong indication that the matrix is indeed a single phase.

Further investigation into the limited matrix activity, which was observed at higher potentials, was performed by cycling two 41 nm $SiN_{0.89}$ cells at a current rate of 62.5 mA/g for 20 cycles, using the same lithiation cut-off as previously at 0.05 V vs. Li^+/Li but with a higher delithiation cutoff of 3 V vs. Li^+/Li. The average 1st cycle reversible capacity of these cells was 1994 mAh/g, which is even a bit higher than the previously estimated total lithium content of the bulk $SiN_{0.89}$ of approximately 1796 mAh/g. This shows that, under these conditions, it is possible to completely delithiate the material, including the matrix, as well as to recover some of the lithium bound in the SEI. This capacity remained stable over the 20 cycles; however, differential capacity analysis (dQ/dV), as seen in Fig. 6, revealed that a significant restructuring of the material occurs during these cycles. During the first few lithiation cycles after the conversion, the dQ/dV plot is dominated
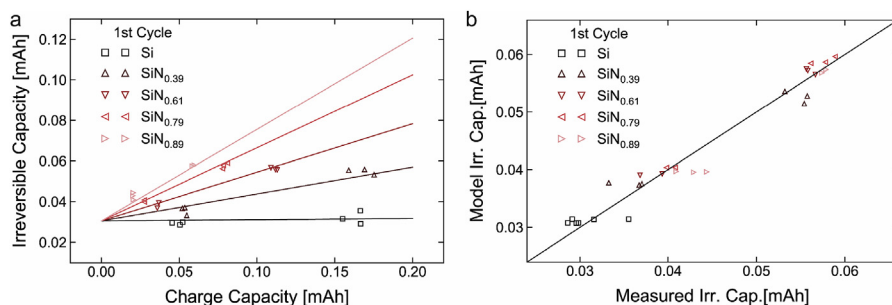

Fig. 3. a) The measured 1st cycle irreversible capacity as a function of the measured 1st cycle charge capacity of the different cells (markers) and the irreversible capacity as determined using equation (7) with the least squares fit parameters and corresponding compositions (lines). b) The modelled 1st cycle irreversible charge capacity as a function of the measured 1st cycle irreversible capacity. The diagonal line represents the points where the two are equal.
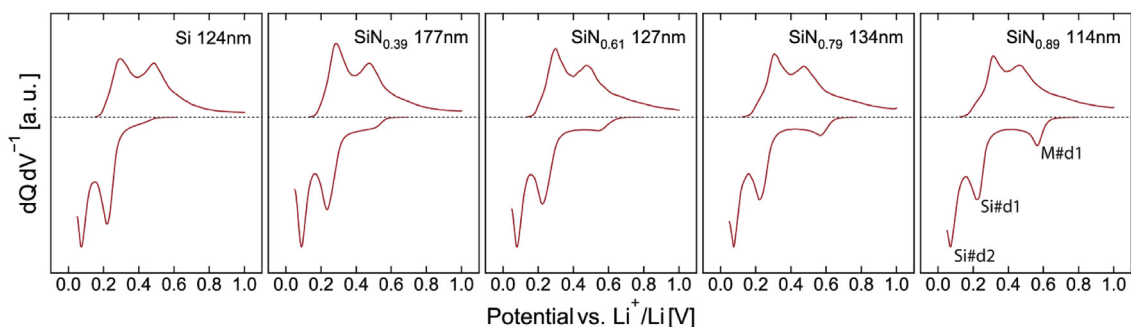
Fig. 4. The differential capacity analysis of the 100th cycle for a number of SiN_x electrodes of different composition cycled between 0.05 and 1 V vs. Li^+/Li.
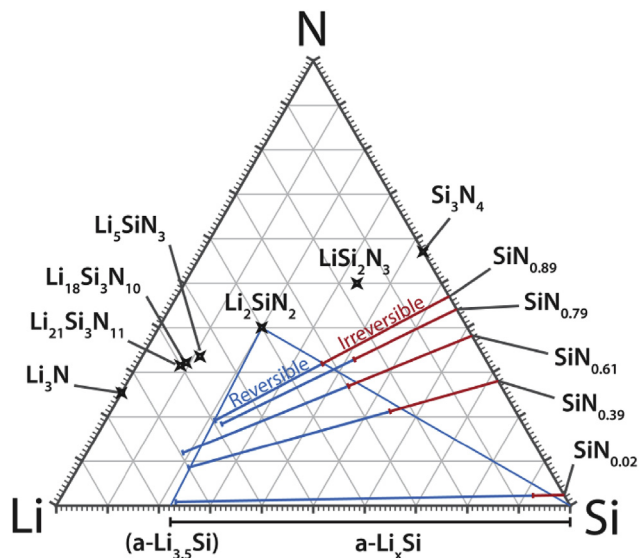

Fig. 5. A constructed lithium-silicon-nitrogen ternary phase diagram, including the known stable ternary phases, showing the lithiation pathways of the different a-SiN_x compositions. The red (right) and blue (left) parts of the lines correspond to the bulk irreversible and reversible capacity, obtained by fitting equations (3) and (4) to the experimental data for each composition. (For interpretation of the references to color in this figure legend, the reader is referred to the Web version of this article.)
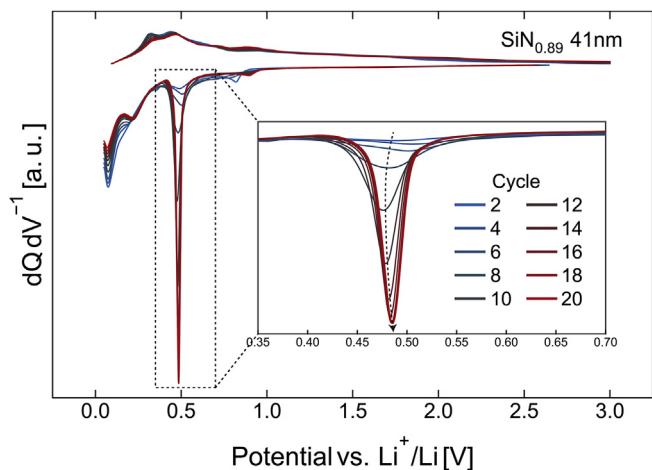

Fig. 6. The differential capacity analysis of a 41 nm $SiN_{0.89}$ electrode cycled between 0.05 and 3 V vs. Li^+/Li.

structure. However, given that the capacities remain largely unchanged, it is expected that the short range coordination distribution of the different species is approximately equivalent, regardless of the long range order. During the subsequent cycles the most prominent change was the intensity reduction of Si#d2 at the benefit of Si#d1 and M#d1. The latter increased markedly for approximately 20 cycles before stabilizing, clearly showing the expected phase separation. During the same cycles, the M#d1 peak position also underwent a slight change, first towards lower voltage for ten cycles before again shifting to higher voltage and stabilizing during the subsequent ten cycles. The initial shift indicates a slight deterioration of the electrode kinetics, which is attributed to a continued SEI formation during these cycles resulting from the high voltage delithiation interfering with normal SEI formation. The subsequent shift towards higher voltage is expected to be a result of improved kinetics in the developing phase separated structure, as has previously been reported for similar thin film electrodes in a related study [48].

The area of M#d1 after stabilization, determined in the manner seen in Fig. 7, corresponds to a capacity of approximately 600 mAh/g. This agrees very well with the predicted matrix contribution to the capacity, which is 590 mAh/g for $SiN_{0.89}$ and a matrix composition of Li_2SiN_2. The sharpness of the peak indicates that the lithiation of the matrix
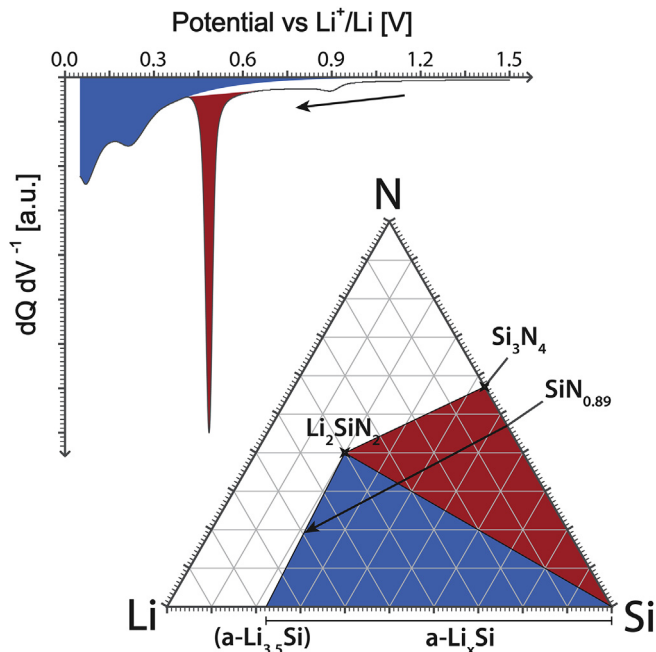

Fig. 7. Illustration of the relationship between the phase diagram and the differential capacity analysis of the 20th lithiation of a $SiN_{0.89}$ electrode cycled between 0.05 and 3 V vs. Li^+/Li. Colors show the corresponding areas of the two figures. (For interpretation of the references to color in this figure legend, the reader is referred to the Web version of this article.)
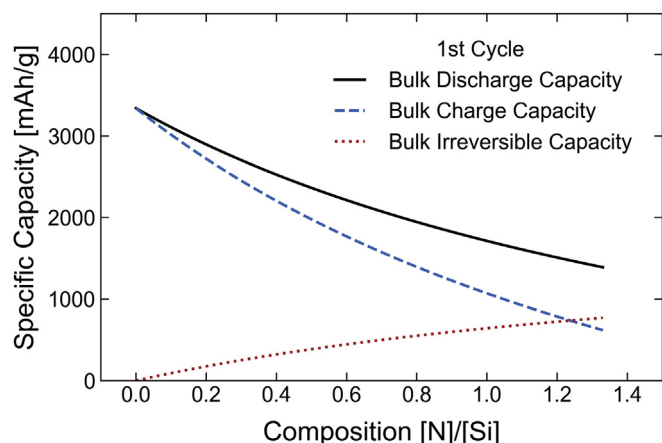
by Si#d2, with only small contributions from Si#d1 and M#d1. This indicates that there is limited long range phase separation, and that most of the lithiation happens by isolation of Si-atoms in the a-SiN_x

Fig. 8. Predicted 1st cycle bulk discharge, charge and irreversible capacities of a-SiN$_x$ as a function of nitrogen content, as determined using the bracketed terms in equations (10) and (11), and their sum, respectively, together with the best fit parameters.

phase is a multi-phase reaction, rather than a gradual lithiation of Li$_x$SiN$_2$, which would rather happen over a potential range. A likely matrix reaction is therefore Si$_3$N$_4$ + 4 Li - > 2 Li$_2$SiN$_2$ + Si. The lack of a similarly sharp peak during delithiation is attributed to a low lithium ion conductivity of the delithiated matrix, which, given that the surface of the film is delithiated first, effectively reduces the kinetics of the further delithiation. Fig. 7 shows an illustration of the relationship between the differential capacity analysis and the phase diagram presented previously. The differential capacity plot is from the 20th lithiation of a SiN$_{0.89}$ electrode after complete delithiation to 3 V vs. Li$^+$/Li. This figure shows how the lithiation path first passes through a three phase region (red), where Si$_3$N$_4$ reacts with lithium to form Li$_2$SiN$_2$ and Si, resulting in the sharp M#d1 peak in the differential capacity plot (red). The lithiation continues into a two phase region (blue), in which Li$_2$SiN$_2$ is a primarily inactive spectator, while silicon is gradually lithiated, first to Li$_2$Si and then to Li$_{3.5}$Si, corresponding to the more diffuse Si#d1 and Si#d2 dQ/dV peaks (blue). The blue features are related to the main reversible reaction when cycling between 0.05 V and 1 V vs. Li$^+$/Li.

Despite the observed slight matrix activity, the plots in Fig. 3 show good agreement between the model and experimental data, demonstrating that the model accurately predicts the reversible capacity and irreversible losses of a nitride with a given composition. By substituting equations (8) and (9) for a and b in equations (3) and (4), we obtain expressions for the expected specific charge capacity and irreversible capacity as functions of nitrogen content (x) in the initial nitride:

$$Cap_{C,\,specific} = \frac{Cap_C}{m} = \left[\frac{(1 - k_1 x)\, 3.5F}{M_{Si} + x M_N} \right] \qquad (10)$$

$$Cap_{I, specific} = \frac{Cap_I}{m} = \left[\frac{k_2 x\, F}{M_{Si} + x M_N} \right] + \frac{cF}{m} \qquad (11)$$

The bracketed terms in these equations represent the first cycle bulk specific irreversible and reversible capacities, and their sum corresponds to the discharge capacity. These capacities, calculated for the predicted matrix composition of Li$_2$SiN$_2$ can be seen as a function of nitride composition in Fig. 8.

4. Conclusions

In this work, we have proposed a model describing the initial nitride conversion reaction in a thin film electrode system. Based on this model, a number of equations have been derived, relating the mass and composition of the electrode with its charge and discharge capacity, as

well as the surface and bulk contributions to the irreversible capacity. Despite the matrix not being completely inactive, we have shown that the equations resulting from this model correlate well with the experimental data, and that this system is well suited for separating surface and bulk contributions to the irreversible losses.

From both a mass dependent and mass independent fitting of experimental data to the model, we determined the Li:Si:N atomic ratio of the matrix to be close to 2:1:2. Based on thermodynamic considerations, we argued that a combination of non-ternary matrix components, e.g. Si$_3$N$_4$ and Li$_3$N, is unlikely, and that the matrix instead consists of the ternary phase Li$_2$SiN$_2$. This was supported by the dQ/dV lithiation-characteristics of the matrix after delithiation to 3.0 V vs. Li$^+$/Li, and is in agreement with a previous study by Suzuki et al. [44]. Based on the determined matrix composition, a prediction of the bulk discharge, charge and irreversible capacity of SiN$_x$ as a function of nitrogen content x was also made, as seen in Fig. 8.

References

[1] W.-J. Zhang, J. Power Sources 196 (2011) 13–24.
[2] L.-F. Cui, R. Ruffo, C.K. Chan, H. Peng, Y. Cui, Nano Lett. 9 (2008) 491–495.
[3] L.-F. Cui, Y. Yang, C.-M. Hsu, Y. Cui, Nano Lett. 9 (2009) 3370–3374.
[4] V. Baranchugov, E. Markevich, E. Pollak, G. Salitra, D. Aurbach, Electrochem. Commun. 9 (2007) 796–800.
[5] S. Bourderau, T. Brousse, D.M. Schleich, J. Power Sources 81–82 (1999) 233–236.
[6] R. Hayakawa, M. Nakae, T. Yoshimura, A. Ashida, N. Fujimura, T. Uehara, M. Tagawa, Y. Teraoka, J. Appl. Phys. 100 (2006) 073710.
[7] M. Ge, J. Rong, X. Fang, A. Zhang, Y. Lu, C. Zhou, Nano Res. (2013) 1–8.
[8] H. Jung, M. Park, S.H. Han, H. Lim, S.-K. Joo, Solid State Commun. 125 (2003) 387–390.
[9] J.P. Maranchi, A.F. Hepp, P.N. Kumta, Electrochem. Solid state Lett. 6 (2003) A198–A201.
[10] J.P. Maranchi, A.F. Hepp, A.G. Evans, N.T. Nuhfer, P.N. Kumta, J. Electrochem. Soc. 153 (2006) A1246–A1253.
[11] T. Takamura, S. Ohara, M. Uehara, J. Suzuki, K. Sekine, J. Power Sources 129 (2004) 96–100.
[12] M. Thakur, M. Isaacson, S.L. Sinsabaugh, M.S. Wong, S.L. Biswal, J. Power Sources 205 (2012) 426–432.
[13] M. Thakur, R.B. Pernites, N. Nitta, M. Isaacson, S.L. Sinsabaugh, M.S. Wong, S.L. Biswal, Chem. Mater. 24 (2012) 2998–3003.
[14] M. Thakur, S.L. Sinsabaugh, M.J. Isaacson, M.S. Wong, S.L. Biswal, Sci. Rep. 2 (2012).
[15] H. Wu, Y. Cui, Nano Today 7 (2012) 414–429.
[16] Y. Zhao, X. Liu, H. Li, T. Zhai, H. Zhou, Chem. Commun. 48 (2012) 5079–5081.
[17] W. Sun, R. Hu, H. Zhang, Y. Wang, L. Yang, J. Liu, M. Zhu, Electrochim. Acta 187 (2016) 1–10.
[18] P. Gao, J. Fu, J. Yang, R. Lv, J. Wang, Y. Nuli, X. Tang, Phys. Chem. Chem. Phys. 11 (2009) 11101–11105.
[19] Y. He, X. Yu, Y. Wang, H. Li, X. Huang, Adv. Mater. 23 (2011) 4938–4941.
[20] A. Kohandehghan, P. Kalisvaart, K. Cui, M. Kupsta, E. Memarzadeh, D. Mitlin, J. Mater. Chem. 1 (2013) 12850–12861.
[21] Z. Lu, N. Liu, H.-W. Lee, J. Zhao, W. Li, Y. Li, Y. Cui, ACS Nano 9 (2015) 2540–2547.
[22] E. Memarzadeh Lotfabad, P. Kalisvaart, K. Cui, A. Kohandehghan, M. Kupsta, B. Olsen, D. Mitlin, Phys. Chem. Chem. Phys.: Phys. Chem. Chem. Phys. 15 (2013) 13646–13657.
[23] A. Ulvestad, J.P. Mæhlen, M. Kirkengen, ECS Trans. 64 (2015) 107–111.
[24] Y. Yu, L. Gu, C. Zhu, S. Tsukimoto, P.A. van Aken, J. Maier, Adv. Mater. 22 (2010) 2247–2250.
[25] I.A. Courtney, J.R. Dahn, J. Electrochem. Soc. 144 (1997) 2045–2052.
[26] Y. Idota, T. Kubota, A. Matsufuji, Y. Maekawa, T. Miyasaka, Science 276 (1997) 1395–1397.
[27] R.A. Huggins, Ionics 3 (1997) 245–255.
[28] R.A. Huggins, Solid State Ionics 152–153 (2002) 61–68.
[29] B. Guo, J. Shu, Z. Wang, H. Yang, L. Shi, Y. Liu, L. Chen, Electrochem. Commun. 10 (2008) 1876–1878.
[30] H. Morimoto, M. Tatsumisago, T. Minami, Electrochem. Solid state Lett. 4 (2001) A16–A18.
[31] J. Yang, Y. Takeda, N. Imanishi, C. Capiglia, J.Y. Xie, O. Yamamoto, Solid State Ionics 152–153 (2002) 125–129.

[32] M. Nishijima, Y. Takeda, N. Imanishi, O. Yamamoto, M. Takano, J. Solid State Chem. 113 (1994) 205–210.

[33] M. Nishijima, N. Tadokoro, Y. Takeda, N. Imanishi, O. Yamamoto, J. Electrochem. Soc. 141 (1994) 2966–2971.

[34] Z.-W. Fu, Y. Wang, X.-L. Yue, S.-L. Zhao, Q.-Z. Qin, J. Phys. Chem. B 108 (2004) 2236–2244.

[35] Y. Wang, Z.-W. Fu, X.-L. Yue, Q.-Z. Qin, J. Electrochem. Soc. 151 (2004) E162–E167.

[36] B.J. Neudecker, R.A. Zuhr, J.B. Bates, J. Power Sources 81–82 (1999) 27–32.

[37] N. Pereira, M. Balasubramanian, L. Dupont, J. McBreen, L.C. Klein, G.G. Amatucci, J. Electrochem. Soc. 150 (2003) A1118–A1128.

[38] I.s. Kim, P.N. Kumta, G.E. Blomgren, Electrochem. Solid State Lett. 3 (2000) 493–496.

[39] M.Q. Snyder, S.A. Trebukhova, B. Ravdel, M.C. Wheeler, J. DiCarlo, C.P. Tripp, W.J. DeSisto, J. Power Sources 165 (2007) 379–385.

[40] X.N. Zhang, G.L. Pan, G.R. Li, J.Q. Qu, X.P. Gao, Solid State Ionics 178 (2007) 1107–1112.

[41] D. Ahn, C. Kim, J.-G. Lee, B. Park, J. Solid State Chem. 181 (2008) 2139–2142.

[42] R.C. de Guzman, J. Yang, M. Ming-Cheng Cheng, S.O. Salley, K.Y.S. Ng, J. Mater. Chem. 2 (2014) 14577–14584.

[43] M. Martín-Gil, M.E. Rabanal, A. Várez, A. Kuhn, F. García-Alvarado, Mater. Lett. 57 (2003) 3063–3069.

[44] N. Suzuki, R.B. Cervera, T. Ohnishi, K. Takada, J. Power Sources 231 (2013) 186–189.

[45] Z. Wen, K. Wang, L. Chen, J. Xie, Electrochem. Commun. 8 (2006) 1349–1352.

[46] C.-Y. Wu, C.-C. Chang, J.-G. Duh, J. Power Sources 325 (2016) 64–70.

[47] A. Ulvestad, H.F. Andersen, J.P. Mæhlen, Ø. Prytz, M. Kirkengen, Sci. Rep. 7 (2017) 13315.

[48] A. Ulvestad, H.F. Andersen, I.J.T. Jensen, T.T. Mongstad, J.P. Mæhlen, Ø. Prytz, M. Kirkengen, Sci. Rep. 8 (2018) 8634.

[49] G.M. Ingo, N. Zacchetti, D.d. Sala, C. Coluzza, J. Vac. Sci. Technol.: Vac. Surface. Films 7 (1989) 3048–3055.

[50] V.A. Volodin, M.D. Efremov, V.A. Gritsenko, S.A. Kochubei, Appl. Phys. Lett. 73 (1998) 1212–1214.

[51] N.-M. Park, C.-J. Choi, T.-Y. Seong, S.-J. Park, Phys. Rev. Lett. 86 (2001) 1355–1357.

[52] V.A. Gritsenko, R.W.M. Kwok, H. Wong, J.B. Xu, J. Non-cryst. Solids 297 (2002) 96–101.

[53] H. Yamane, S. Kikkawa, M. Koizumi, Solid State Ionics 25 (1987) 183–191.

[54] K. Ogata, E. Salager, C.J. Kerr, A.E. Fraser, C. Ducati, A.J. Morris, S. Hofmann, C.P. Grey, Nat. Commun. 5 (2014).

[55] I. Schreinlechner, F. Holub, Compatibility of certain ceramics with liquid lithium, in: H.U. Borgstedt (Ed.), Material Behavior and Physical Chemistry in Liquid Metal Systems, Springer US, Boston, MA, 1982, pp. 105–111.

[56] B. Key, M. Morcrette, J.-M. Tarascon, C.P. Grey, J. Am. Chem. Soc. 133 (2011) 503–512.

[57] B. Key, R. Bhattacharyya, M. Morcrette, V. Seznéc, J.-M. Tarascon, C.P. Grey, J. Am. Chem. Soc. 131 (2009) 9239–9249.

Glossary

DMC: Dimethyl carbonate
EC: Ethylene carbonate
EELS: Electron energy loss spectroscopy
FEC: Fluoroethylene carbonate
FIB: Focused ion beam
PC: Propylene carbonate
PECVD: Plasma enhanced chemical vapor deposition
SEI: Solid electrolyte interphase
SEM: Scanning electron microscopy
STEM: Scanning transmission electron microscopy
TEM: Transmission electron microscopy
VC: Vinylene carbonate
XPS: X-ray photoelectron spectroscopy